Catal Lett (2007) 118:1–7
DOI 10.1007/s10562-007-9162-1

Size Dependent Study of MeOH Decomposition Over Size-selected Pt Nanoparticles Synthesized via Micelle Encapsulation

**Jason R. Croy · Simon Mostafa · Jing Liu ·
Yong-ho Sohn · Beatriz Roldan Cuenya**

Received: 15April 2007 / Accepted: 26 April 2007 / Published online: 11 July 2007

Abstract We present here the size-dependent decomposition of methanol (MeOH) over narrowly distributed Pt nanoparticles supported on nanocrystalline anatase TiO_2 powder. Micelle encapsulation has been used to create Pt catalysts with average particle sizes of ~4, 6, and 8 nm. A packed bed mass flow reactor and mass spectrometry were employed to quantify the catalyst's activity and selectivity. Among the catalysts tested the smallest nanoparticles showed the best performance including an onset reaction temperature of ~145 °C. No byproducts such as CO_2 or CH_4 were observed in the test range of 100–330 °C.

Keywords Methanol decomposition · MeOH · H_2 production · Micelles · Pt · Nanoparticle · TiO_2 · Catalysis · XPS · TEM · AFM · Mass flow reactor · Mass spectrometry

1 Introduction

Presently, with the world's demand for energy projected to double by the year 2050 [1], the development of enabling technologies for alternative energy sources is no longer a question of debate but rather one of necessity. Hydrogen is seen as one of the most promising alternatives and can be produced in a myriad of ways [2]. The quest for a hydrogen economy has attracted much attention to the reforming of liquid hydrocarbons, and in particular to the reforming of methanol. Because of its adaptability to the existing infrastructure, and high hydrogen density, methanol is seen as one of the most viable options for widespread use in fuel cell vehicles [3]. Methanol can be produced from a number of renewable resources such as black liquor, animal waste, and dedicated energy crops, giving it environmental as well as economic appeal.

The decomposition of methanol for the production of synthesis gas ($CO/CO_2/H_2$) has many industrially relevant applications such as the production of high-purity hydrogen for metallurgical processes, generation of electricity, and its promise for use in fuel cell technology, thus it has been the subject of intensive study [4, 5]. There are several decomposition processes currently in use and under study including direct decomposition, steam reforming, and oxidation [5]. These processes require the use of metallic nanoparticle catalysts such as Cu, Pt, and Pd supported on various metal oxides [6]. In the reverse direction, the synthesis of methanol is a process that is better understood in that there is now a preferred catalyst in widespread industrial use ($Cu/ZnO/Al_2O_3$) [7]. However, the reaction site and pathway mechanisms of this catalyst are still under investigation [7–9]. Recently, other metals such as Ag, Au, and AuPt alloys have shown potential as active catalysts for methanol synthesis and oxidation [10, 11].

Metallic nanoparticles having dimensions less than 10 nm have been found to have size dependent chemical reactivity, due in part to quantum size effects and an increase in step density with decreasing particle size [12–14]. It has been shown that irregularities, such as kinks and steps, play a vital role in catalytic reactions that occur at surfaces [15]. In particular, the physical and electronic properties of a nanoparticle catalyst are greatly affected by

J. R. Croy · S. Mostafa · B. Roldan Cuenya (✉)
Department of Physics, University of Central Florida, Orlando, FL 32816, USA
e-mail: roldan@physics.ucf.edu

J. Liu · Y.-h. Sohn
Department of Mechanical, Material, and Aerospace Engineering, Advanced Materials Processing and Analysis Center, University of Central Florida, Orlando, FL 32816, USA

the number of atoms that make up such a catalyst. As the particle size becomes smaller, the surface to volume ratio grows, and the number of low coordinated surface atoms grows accordingly. Such under-coordinated sites are known to display distinct electronic properties. As an example, a local enhancement of the electron density of states has been measured by scanning tunneling microscopy (STM) at surface steps [16]. A possible correlation between the unusual electronic features of low coordinated atoms in nanoparticles and their increased catalytic reactivity is under investigation.

Pt nanocatalysts have been proven to be exceptionally active and selective for many industrially relevant chemical reactions including hydrogen evolution [17], methanol decomposition [18], the partial oxidation of methane [19], ethylene hydrogenation [20], and the abatement of automobile emissions, which includes CO oxidation as well as the reduction of hydrocarbons and NO_x [21]. The nanoparticle synthesis method of micelle encapsulation allows precise control over the size, shape, and spatial distribution of particles [15], making it an attractive candidate for the synthesis of monodispersed nanocatalysts. This is especially critical in fuel cell technologies where expensive noble metals, such as Pt, are required to achieve not only enhanced activity but also selectivity, which has become the focus of modern catalysis [22, 23]. In this paper we present the size dependence of methanol decomposition over Pt nanoparticles synthesized by micelle encapsulation and supported on polycrystalline anatase TiO_2 powder.

2 Experimental

Non-polar/polar diblock copolymers [Poly(styrene)-block-poly(2vinylpyridine)] were dissolved in a non-polar solvent (toluene) in order to obtain spherical nano-cages (inverse micelles). The micelles were then loaded with a metal salt ($H_2PtCl_6 \cdot 6H_2O$) to produce self-confined and size-selected Pt nanoparticles. The particle size can be tuned by using polymers with different head lengths and/or by changing the metal-salt/polymer head concentration in the solution [24–26]. The solution was then mixed with TiO_2 in the form of a powder and placed in a tubular furnace open to the air for calcination. For these experiments the catalyst powder was not sieved. The nominal size of the nanocrystalline anatase TiO_2 support (Alfa Aesar) was ~32 nm, with our TEM data giving an average particle diameter of ~42 nm after annealing at 500 °C for 2.5 h. Each Pt/TiO_2 catalyst sample had a total weight of 150 mg and contained 2% by weight Pt. The amount of Pt salt used in each sample is derived from the Pt-salt/P2VP ratio as reported in Table 1. In these experiments three commercial polymers [PS(x)-b-P2VP(y), Polymer Source Inc.], having head groups with different molecular weights, were used in order to create three distinct particle sizes. Further sample preparation details can be found in Table 1.

Powder samples were deposited on carbon conductive tabs (Ted Pella, Inc.) and transferred to an ultra high vacuum system (UHV, SPECS GmbH) for surface analysis by X-ray photoelectron spectroscopy (XPS). XPS data were collected using a monochromatic X-ray source (Al-Kα, 1,486.6 eV) operating at 400 W. The binding energies of all samples were referenced to the Ti $2p_{3/2}$ [TiO_2] peak at 458.6 eV [27].

To study the effect of calcination on the activity of the catalyst, as well as to remove the encapsulating PS-PVP polymers, the samples were annealed before the reaction at two different temperatures. One set of samples was annealed at 315 °C for 3 h and another set at 500 °C for 2.5 h. Activity tests were then conducted on each of the sample sets.

Catalytic decomposition of methanol in the vapor phase was carried out in a packed bed mass flow reactor. A vertical quartz tube (inside diameter 4 mm) served as the reactor vessel and the 150 mg powder catalysts were supported between glass wool plugs, giving a bed height of ~3.5 cm. A thermocouple (K-type) in contact with the reactor at the location of the catalyst was used to monitor temperature and the entire assembly was insulated to minimize heat losses. Immediately prior to the reaction all catalysts were heated for 1 h at ~200 °C (below the initial calcination temperatures) in a flow of He at 10 mL/min. Activities were measured at atmospheric pressure in the range of 100–330 °C . The temperature was increased stepwise and kept constant at the recorded values. Regions of stable activity were obtained and averaged over ~3–5 min intervals. Helium was used as the carrier gas during methanol decomposition. The He flow was regulated by a mass flow controller (MKS) at 10 mL/min. The composition of the feed was 2% MeOH, relative to the flow of He as determined by the partial pressures of He and the main fragment ion of MeOH (mass 31). The product stream of the reactor was monitored by a quadrupole mass spectrometer (Hiden HPR-20, QMS). The QMS is equipped with a heated silica capillary (inside diameter 0.3 mm) from which the sample gases exit at low pressure and high velocity, and subsequently impinge on a platinum orifice (diameter 0.02 mm). The orifice provides a second stage of pressure reduction from which sample gases enter directly into the mass spectrometer ion source. The inlet of the capillary has a maximum consumption of 16 mL/min. Several tests involving the flow of the carrier gas were carried out until an optimum flow of 10 mL/min was selected for our experiments. This setup can be operated in a pressure range of 10 mbar–2 bar. Partial pressures of all gases were monitored using the system's Faraday cup detector.

Table 1 Synthesis parameters and average height (AFM) and diameter (TEM) distributions of Pt nanoparticles synthesized by inverse micelle encapsulation

Sample	PS(*x*)/P2VP(*y*) molecular weight (g/mol)	Pt(salt)/P2VP ratio	Annealing (°C)	AFM height (nm)	TEM diameter (nm)
# 1	27,700/4,300	0.6	500	3.7 ± 0.6 nm	8.6 ± 1.2 nm[a] 8.2 ± 1.7 nm[b]
# 2	27,700/4,300	0.6	315	–	–
# 3	53,400/8,800	0.3	500	6.3 ± 1.1 nm	20.8±2.7 nm[a]
# 4	53,400/8,800	0.3	315	–	–
# 5	81,000/14,200	0.6	500	8.1 ± 1.4 nm	11.4 ± 1.6 nm[a]
# 6	81,000/14,200	0.6	315	–	–

Here the symbol [a] represents size distributions of the samples measured after annealing but before exposure to methanol, and [b] represents distributions done after annealing and subsequent exposure to methanol

The polymer-salt solutions were also dip-coated on SiO_2/Si(001) substrates in order to obtain particle size information (height) via atomic force microscopy (AFM) with a Nanoscope Multimode^{TM} (Digital Instruments) microscope operating in tapping mode. In addition, transmission electron microscopy (TEM) was carried out on the powder samples with a Tecnai F30 TEM operating at an accelerating voltage of 300 kV.

3 Results and Discussion

3.1 Morphological and Structural Characterization

Figure 1 displays AFM images of the three different polymer-salt solutions dip-coated on SiO_2/Si(001) before (left) and after (right) UHV annealing for 30 min at 500 °C. At this temperature removal of the encapsulating polymer is observed by monitoring the C-1s XPS signal. As seen in Fig. 1, the size distribution in each sample is narrow, demonstrating that the simple method of micelle encapsulation can consistently synthesize size-selected Pt nanoparticles. Analysis of the images taken after annealing gives an average particle height of 3.7 ± 0.6 nm (b), 6.3 ± 1.1 nm (d), and 8.1 ± 1.4 nm (f). Since the nanoparticle diameters measured are significantly enhanced due to tip-convolution effects, the AFM heights measured will be used as the representative size of the nanoparticles throughout the text.

Figure 2 shows typical bright-field TEM images of Pt nanoparticles prepared by micelle encapsulation, which are supported on anatase TiO_2 powder. Contrasts from these images were also employed to measure the size of the Pt nanoparticles as reported in Table 1.

3.2 Electronic and Chemical Characterization

Figure 3 shows XPS spectra of the Pt region for three samples annealed at 315 °C (samples #2, #4, #6) and three samples annealed at 500 °C (samples #1, #3, #5) before reaction with methanol. The solid lines indicate the positions of the main core-level peaks of metallic Pt at 70.4 eV ($4f_{7/2}$) and 73.7 eV ($4f_{5/2}$) [28], the dashed lines to Pt^{2+} in PtO (72.4 and 75.7 eV) [29], and the dotted lines to Pt^{4+} in PtO_2 (74.6 and 77.9 eV) [30].

All samples annealed at 315 °C display a convolution of mainly Pt^0 and Pt^{2+}. Since a residual Cl signal was measured after this low temperature (315 °C) thermal treatment for samples #2, #4, and #6 (Fig. 4 shows Cl 2p XPS data from sample #2), we conclude that the Pt^{2+} found in these samples must be mainly in chlorinated compounds. This is in agreement with the binding energies measured by Zhao et al. [31] on dendrimer-encapsulated Pt nanoparticles before the removal of the encapsulating ligands (72.8 and 75.7 eV). Furthermore, in these samples the Pt^{2+}/Pt^0 ratio was found to increase with increasing particle size. In particular, the XPS spectrum from the sample containing the largest nanoparticles (sample #6) shows mainly Pt^{2+}—4f peaks at ~72.4 and 75.7 eV. The difference in the Cl content of nanoparticle samples with different sizes (higher Cl content for larger clusters) can be tentatively attributed to the different number of low-coordinated Pt atoms in these systems, as well as to the distinct melting temperature of clusters with different sizes. Small clusters have a larger number of atoms at the surface and a reduced melting temperature. It is therefore plausible that chlorinated compounds in such systems, available mainly at the nanoparticle surface, are easier to decompose upon thermal treatment. For larger clusters, the complete Cl removal from the bulk requires higher annealing temperatures as well as longer annealing times. Upon annealing to 500 °C (samples #1, #3, #5), no residual Cl signal was observed (Fig. 4, sample #1) and the binding energies measured were attributed to Pt^0, PtO, and PtO_2. After identical thermal treatments, it was found that the oxidation state of the nanoparticles depends on the particle size. The smallest nanoparticles (sample #1) were fully reduced at 500 °C, while samples #3 and #5 still contained Pt^{2+} and

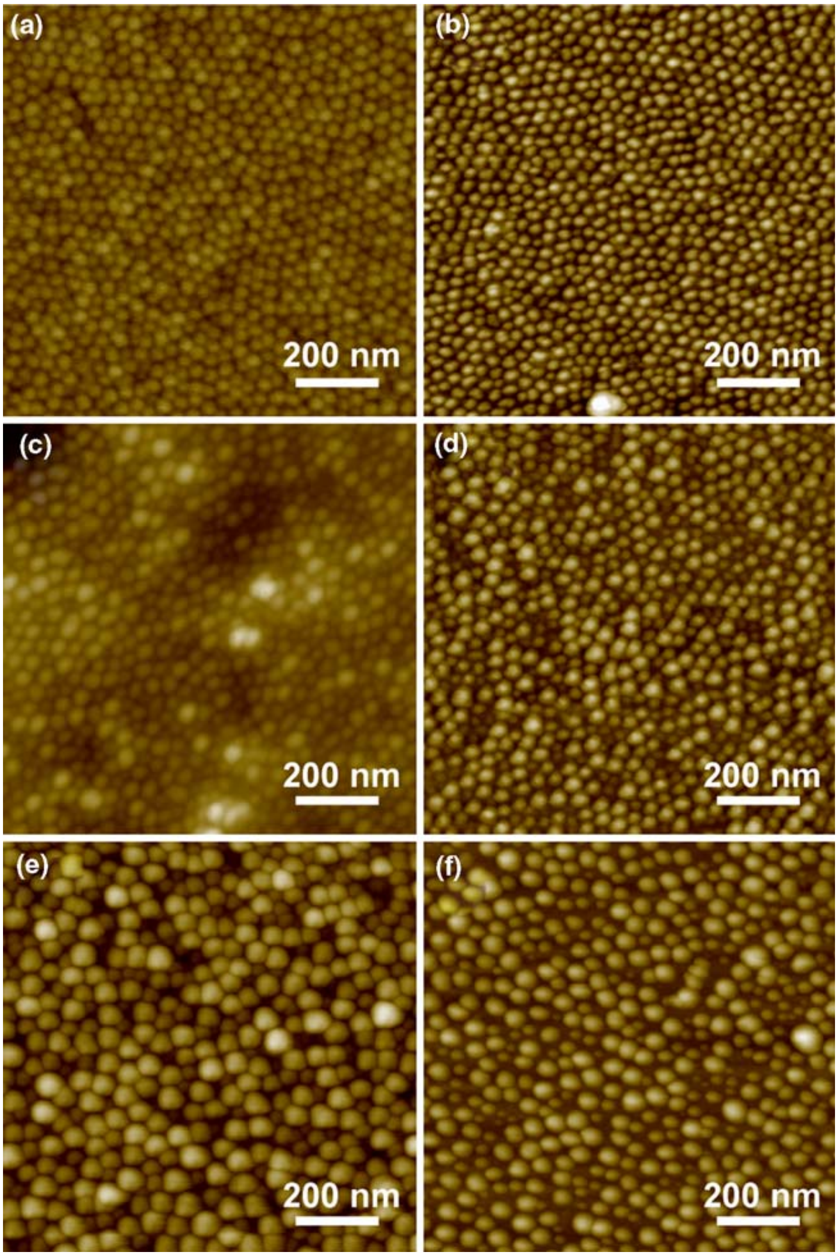

Fig. 1 Tapping mode AFM images of size-selected Pt nanoparticles dip-coated on SiO_2/Si(001). The left column shows samples #1 (**a**), #3 (**c**), and #5 (**e**) before annealing. The right column shows samples #1 (**b**), #3 (**d**), and #5 (**f**) after annealing in UHV at 500 °C for 30 min. The z scale is 0–12 nm for (**b**), 0–25 nm for (**f**), and 0–20 nm for all others

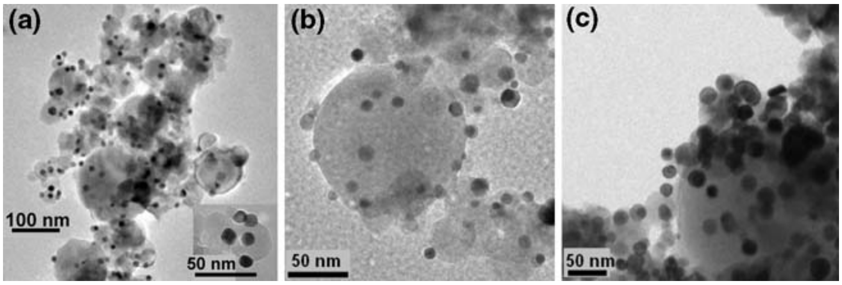

Fig. 2 Bright-field TEM images showing Pt nanoparticles prepared by micelle encapsulation supported on anatase TiO_2 powder: (**a**) sample #1 before reaction with methanol and (**b**) sample #1 after methanol exposure, (**c**) sample #3 before reaction with methanol. All samples shown were calcined at 500 °C

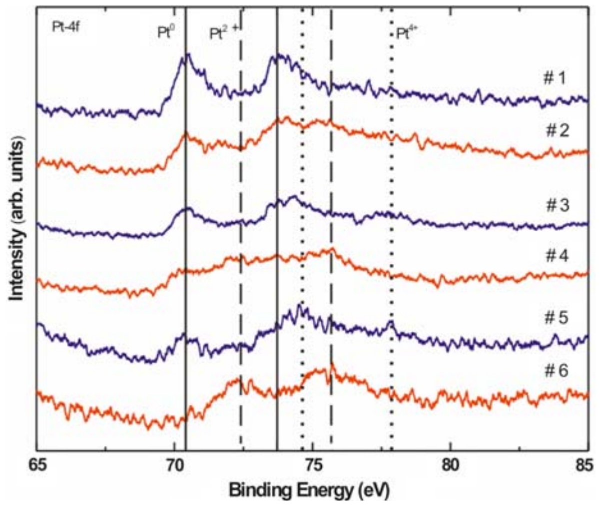

Fig. 3 XPS spectra of Pt particles supported on TiO_2 measured at room temperature. The solid lines show the positions of the 4f peaks of metallic Pt, the dashed lines give the positions of the Pt^{2+} peaks, and the dotted lines show Pt^{4+}. The spectra number at the right corresponds to the sample from which the data were obtained and is described in Table 1

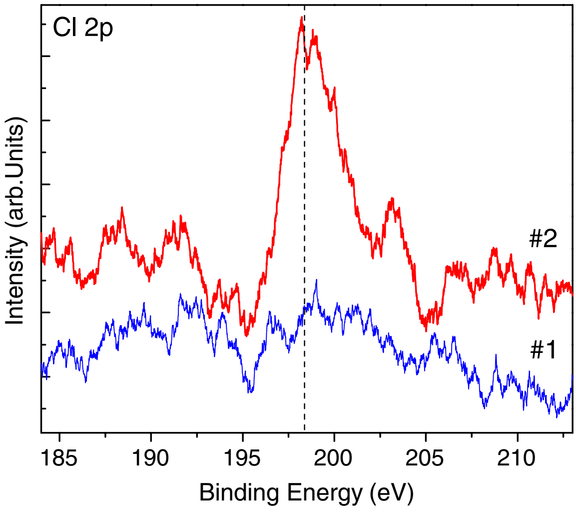

Fig. 4 XPS data showing Cl 2p at ~198.4 eV. All samples show residual Cl after calcination at 315 °C (sample #2 is shown here). After calcination at 500 °C the Cl is removed and all samples show spectra similar to that of sample #1 as shown in the figure

Pt^{4+} compounds. It is interesting to note that the main Pt peak ($4f_{7/2}$) of all samples appears at ~70.4 eV. This value is close to those reported by Silvestre-Albero et al. [32] for similar TiO_2-supported Pt particles, and corresponds to a negative shift of ~0.7 eV when compared to the most common value measured for bulk Pt^0 at 71.1 eV [33]. Such negative shifts can be explained by strong support-metal interactions. Charge transfer from the support to the particle, especially in systems with metallic particles on reducible metal oxides, can alter the electronic properties of the particle [34]. Small particles also have a large number of surface atoms with reduced coordination number. This feature is known to induce negative binding energy shifts relative to the value measured for the bulk metal [35].

3.3 Catalytic Activity

Figure 5 displays the activity as calculated from data acquired by the quadrupole mass spectrometer. Activity is defined in terms of partial pressures measured by the QMS and given by the equation $(PH_2–PH_0)/P_{m31}$. Here PH_2 is the pressure of H_2 at a given temperature, PH_0 is the initial background pressure of H_2, and P_{m31} is the pressure of the main fragment ion of methanol. A clear size dependence of the catalytic activity of Pt nanoparticles supported on TiO_2 is observed. For the sample set annealed at 315 °C (open symbols in Fig. 5) we can see a well-defined trend where an increase in activity is associated with a decrease in particle size. A similar trend was observed for the set of samples annealed at 500 °C (closed symbols in Fig. 5), although samples #3 and #5 displayed almost identical activities. This effect can be attributed to nanoparticle coarsening, since our TEM measurements indicate that significant agglomeration occurred in sample #3 after annealing at 500 °C (Fig. 2), rendering an average size distribution comparable to sample #5. Furthermore, the most dramatic improvement in activity was observed for the largest particles (sample #5) after the high temperature pre-treatment. This may be related to the fact that the

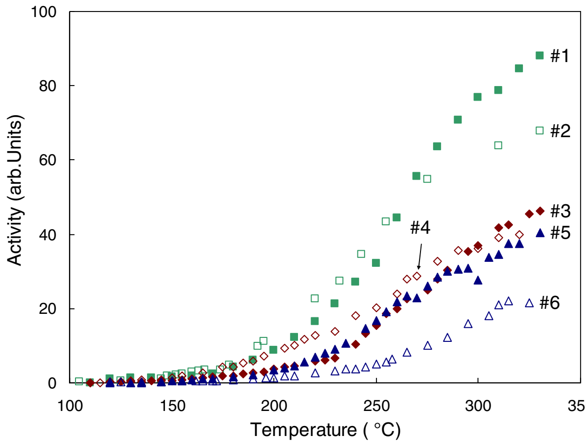

Fig. 5 Activity of size-selected Pt nanoparticles supported on TiO_2 anatase powder (see Table 1 for details) for methanol decomposition. The activity is defined in terms of partial pressures measured by a quadrupole mass spectrometer (QMS) and given by the equation $(PH_2-PH_0)/P_{m31}$. Here PH_2 is the pressure of H_2 at a given temperature, PH_0 is the initial background pressure of H_2, and P_{m31} is the pressure of the main fragmention of methanol. Samples are identified by their number as given in Table 1

analogous sample, annealed at 315 °C (sample #6), showed the largest Pt^{2+}/Pt^0 ratio, and that subsequent annealing to 500 °C served to remove residual Cl and increase the amount of metallic Pt species. The other two sizes annealed at 500 °C also displayed enhanced activities as the temperature in the reactor approached 260 °C for sample #1 and 300 °C for sample #3. This suggests that after low temperature annealing (315 °C) there is residual Cl in the samples which is detrimental to the reaction, and that the higher annealing temperature is of greater advantage as long as the sintering is minimized. Our mass spectroscopy data from samples #3 and #4 indicate that any benefits gained from the removal of the chlorine can be offset by a corresponding increase in particle size. This size effect also reveals itself in the low temperature region of Fig. 5, where we see a clear decrease in activity for sample #3 as compared to its counterpart (sample #4) calcined at lower temperature (315 °C).

We also note that all samples show H_2 production well below 200 °C with the smallest particles (sample #1) becoming active when the reactor temperature is about 145 °C. This is especially important for the development of heat recovery systems [36] and compares favorably with values reported elsewhere [37–41]. During the course of all reactions no significant amount of byproducts such as methane (CH_4), carbon dioxide (CO_2), or dimethyl ether (CH_3OCH_3) were observed. Therefore, the main process involved is the direct decomposition of MeOH and competing H_2 reactions (i.e. methanation) are not a factor.

Figure 5 shows that the smallest particles, which were also more easily reduced from $Pt^{\delta+}$ to Pt^0, displayed the highest activities. This effect is further illustrated in Fig. 6 where the activity, measured at four different reaction temperatures for samples calcined at 500 °C (samples #1, #3 and #5), is plotted versus the nanoparticle height as measured by AFM. Here again we can see the effects of increased nanoparticle size in sample #3, which shows a slightly lower activity than sample #5 at 250 °C (squares), and is comparable to sample #5 even at 300 °C (diamonds). Thus, the removal of the Cl from this sample has been negated by an increase in particle size. We conclude that nanoparticle coarsening in sample #3 is not due to temperatures in the reactor since all experiments were conducted in the range of 100–330 °C, which is well below the pretreatment temperature of samples #1, #3, and #5 at 500 °C. In addition, TEM analysis reveals that the most active particles (sample #1) did not coarsen during reaction with methanol, having an average size of 8.6 ± 1.2 nm before reaction, and 8.2 ± 1.7 after reaction (Table 1). We may note also that each experiment lasted for about 6 h, and no deactivation was observed during that period of time for any sample.

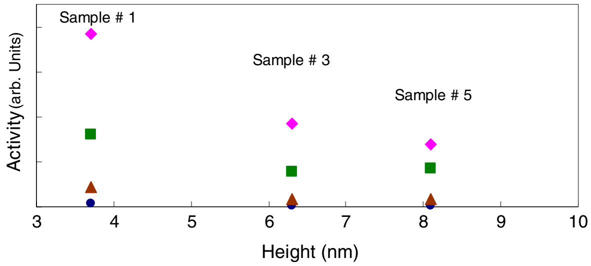

Fig. 6 Activity plotted as a function of particle height (AFM) at four different reaction temperatures for samples previously calcined at 500 °C (samples #1, #3 and #5). Circles represent a reactor temperature of 150 °C, triangles 200 °C, squares 250 °C, and diamonds 300 °C. Columns are denoted by the sample number as given in Table 1

On similarly synthesized gold nanoparticles supported on TiC, our group has also demonstrated a dependence of the particle size on the catalytic activity of this system for low temperature CO oxidation [15]. However, we must mention that smaller particles do not always perform better, and reducing particle size may only be advantageous to a point. For example, It is known that a minimum number of atoms per cluster is required to observe high reactivities, in particular the enhanced activities displayed by small clusters for CO oxidation decrease below a particle size of about 2–3 nm [13, 42].

Although the present study focuses on the influence of the nanoparticle size on chemical reactivity, it should be stated that the nature of the metal oxide support also plays a crucial role in catalytic processes mediated by supported nanoparticles. For example, the use of ZnO, TiO_2, SiO_2, CeO_2, and Al_2O_3 as supports can effect particle sintering, catalytic activity, and selectivity in reactions such as MeOH decomposition [43], steam reforming of MeOH [44], and CO oxidation and propylene hydrogenation [45]. It is believed that the oxygen vacancies that easily appear in some of these materials upon annealing may play a crucial role [46, 47]. More specifically, on reduced TiO_2, charge redistribution and accumulation around oxygen vacancies has been predicted [34], and the possibility of charge transfer to small nanoparticles suggested. This excess charge could significantly influence the catalytic performance of the cluster/metal oxide system.

4 Conclusion

Micelle encapsulation has been used to create size-selected Pt nanoparticles highly dispersed on polycrystalline anatase-TiO_2 supports. These nanocatalysts were found to be active for the decomposition of MeOH and subsequent production of H_2 at temperatures as low as 145 °C. Mass spectrometry data show that on these Pt nanoparticles H_2

production proceeds mainly through the direct decomposition of MeOH and that the activity increases with decreasing particle size. Furthermore, the influence of the oxidation state of the Pt nanoparticles on their activity and selectivity was investigated. Our mass spectrometry data reveal that the samples annealed at higher temperature, where a larger percentage of metallic Pt species was detected by XPS, are the most active. However, this is not the case when the high temperature treatment leads to nanoparticle coarsening and significant increase in particle size. In addition, the residual Cl present in our catalysts after low temperature annealing (315 °C) was found to hinder the reaction. However, the size of the particles turned out to be the dominant factor in determining the relative activity of these samples, and the smallest Pt nanoparticles were found to be the most active.

Acknowledgments We gratefully acknowledge the support of this work by the Donors of the American Chemical Society Petroleum Research Fund under Grant PRF-42701-G5 and supplement for minority undergraduate summer research, and the National Science Foundation (NSF-CAREER award, No. 0448491). J. Croy would like to thank Dr. Ahmed Naitabdi and Luis Ono for their technical assistance.

References

1. U.S. Department of Energy (2003) Basic research needs for solar energy utilization
2. Norskov JK, Christensen CH (2006) Science 312:1322
3. Olah GA (2004) Catal Lett 93:1
4. Haruta M, Souma Y (1997) Catal Today 36:1
5. Spencer MS (2003) Top Catal 22:135
6. Zhang XH, Luo LT, Duan ZH (2005) React Kinet Catal Lett 87:43
7. Tabatabaei J, Sakakini BH, Waugh KC (2006) Catal Lett 110:77
8. Kurtz M, Strunk J, Hinrichsen O, Muhler M, Fink K, Meyer B, Woell C (2005) Angew Chem Int Ed 44:2790
9. Wilmer H, Kurtz M, Klementiev KV, Tkachenko OP, Grunert W, Hinrichsen O, Birkner A, Rabe S, Merz K, Driess M, Wöll C, Mühler M (2003) Phys Chem Chem Phys 5:4736
10. Sakahara S, Yajima K, Belosludov R, Takami S, Kubo M, Miyamoto A (2002) Appl Surf Sci 189:253
11. Lou Y, Maye MM, Han L, Luo J, Zhong CJ (2001) Chem Comm 5:473
12. Mavrikakis M, Stoltze P, Norskov J, (2000) Catal Lett 64:101
13. Valden M, Lai X, Goodman DW (1998) Science 281:1647
14. Haruta M (1997) Catal Today 36:153
15. Ono LK, Sudfeld D, Roldan Cuenya B (2006) Surf Sci 600:5041
16. Schneider A, Wenderoth M, Engel KJ, Rosentreter MA, Heinrich AJ, Ulbrich RG (1998) Appl Phys A Mat Sci Process 66:S161
17. Hinnemann B, Moses PG, Bonde J, Jorgensen KP, Nielsen JH, Horch S, Chorkendorff I, Norskov JK (2005) J Am Chem Soc 127:5308
18. Brown JC, Gulari E (2004) Catal Commun 5:431
19. Passos FB, Oliveira ER, Mattos LV, Noronhe FB (2006) Catal Lett 110:261
20. Jacobs PW, Ribeiro FH, Somorjai GA, Wind SJ (1996) Catal Lett 37:131
21. Farrauto RJ, Heck RM (1999) Catal Today 51:351
22. Freund HJ, Libuda J, Baumer M, Risse T, Carlsson A (2003) Chem Rec 3:181
23. Somorjai GA, McCrea K (2001) Appl Catal A 222:3
24. Glass R, Arnold M, Blummel J, Kuller A, Möller M, Spatz JP (2003) Adv Funct Mater 13:569
25. Jaramillo TF, Baeck SH, Roldan Cuenya B, McFarland EW (2003) J Am Chem Soc 125:7148
26. Roldan Cuenya B, Baeck SH, Jaramillo TF, McFarland EW (2003) J Am Chem Soc 125:12928
27. Bond GC, Flamerz S (1989) Appl Catal 46:89
28. Duckers K, Bonzel HP (1989) Surf Sci 213:25
29. Bancroft GM, Adams I, Coatsworth LL, Bennewitz CD, Brown JD, Westwood WD (1975) Anal Chem 47:586
30. Kim KS, Winograd N, Davis RE, (1971) J Am Chem Soc 93:6296
31. Zhao M, Crooks RM (1999) Adv Mater 11:217
32. Silvestre-Albero J, Sepulveda-Escribano A, Rodriguez-Reinoso F, Anderson JA (2004) J Catal 223:179
33. Fierro JLG, Palacios JM, Tomas F (1988) Surf Interface Anal 13
34. Laurent S, Linic S (2006) Phys Rev Lett 97
35. Bjorneholm O, Federmann F, Fossing F, Möller T (1995) Phys Rev Lett 74:3017
36. National Research Council (1992) Catalysis looks to the future, Washington DC
37. Usami Y, Kagawa K, Kawazoe M, Matsumura Y, Sakurai H, Haruta M (1998) Appl Catal A 171:123
38. Shen WJ, Matsumura Y (2000) Phys Chem Chem Phys 2:1519
39. Kapoor MP, Ichihashi Y, Kuraoka K, Shen WJ, Matsumura Y (2003) Catal Lett 88:83
40. Matsumura Y, Tanaka K, Tode N, Yazawa T, Haruta M (2000) J Mol Catal A 152:157
41. Liu YY, Suzuki K, Hamakawa S, Hayakawa T, Murata K, Ishii T, Kumagai M (2000) Catal Lett 66:205
42. Lai X, Goodman DW (2000) J Molec Catal A 162:33
43. Antonyuk SN, Lapidus AL, Kazanskii VB, Yakerson VI, Khanumyan AA, Golosman EZ, Nechugovskii AI, Pesin OYu (2000) Kinet Catal 41:831
44. Men Y, Gnaser H, Zapf R, Hessel V, Ziegler C (2004) Catal Comm 5:671
45. Chou J, Franklin NR, Baeck S, Jaramillo TF, McFarland EW (2004) Catal Lett 95:107
46. Campbell CT, Peden CHF (2005) Science 309:713
47. Esch E, Fabris S, Zhou L, Montini T, Africh C, Fornasiero P, Comelli G, Rosei R (2005) Science 309:752